Aerodynamics of a stay cable with helical fillets - Part II: Fluctuating load and wake characteristics

H. Christiansen [a,1,*], J.B. Jakobsen [a], J.H.G. Macdonald [b], G.L. Larose [c,2], H.R. Bosch [d]

[a] Department of Mechanical and Structural Engineering and Material Science, University of Stavanger, Norway
[b] Department of Civil Engineering, University of Bristol, UK
[c] National Research Council Canada, 1200 Montreal Road, Ottawa, Ontario, Canada
[d] Aerodynamics Laboratory, Federal Highway Administration, McLean, VA, USA

ARTICLE INFO

ABSTRACT

This paper presents the fluctuating load and wake characteristics of a bridge stay cable model with helical fillets in smooth flow at high Reynolds numbers. Over the Reynolds numbers tested, the frequency content of the lift coefficient in individual pressure tap rings, was dominated by low frequencies. At lower Reynolds numbers, these were caused by single separation bubble instabilities. At smaller spectral magnitudes, a vortex shedding process was observed, with a local Strouhal number dependent on the angular position of the helical fillet nearly normal to flow. For the average over the four rings, the low frequencies cancelled out, and left a high frequency vortex shedding process with a Strouhal number of 0.19 as the prominent load. The Strouhal number was maintained throughout the Reynolds number range tested. In dynamic tests, the pressure distribution was found to periodically rotate relative to the cable circumference at the natural frequency of the cable. Also, when observing the velocity components in the wake, a periodic motion of the wake synchronized with the cable motion was revealed. In static tests, the wake field instantly displaced towards the same side as the lift force generated by the asymmetric pressure distribution during boundary layer instabilities.

1. Introduction

Bridge stay cables have been reported to suffer from different vibration problems such as rain-wind induced vibrations (RWIV), buffeting, dry inclined cable vibrations etc., whereof the former is most frequently observed. In the search to mitigate RWIV the helical fillet was developed and the first application of helical fillets to bridge stay cables were on the Normandy Bridge in France, Flamand (1995). This passive aerodynamic solution has since been widely utilised. However, recently there has been growing concerns regarding the aerodynamics of cables with helical fillets in dry weather conditions, as this case has not been studied and because dry inclined cable vibrations have been observed on-site for cables with smooth high-density-polyethylene (HDPE) pipes, see e.g. Zuo and Jones (2010). This led to the experimental research study presented in this and the companion paper Christiansen et al. (2017) carried out at the National Research Council Canada (NRC) in 2011. In the wind tunnel experiments the aerodynamic stability of a bridge cable model with

helical fillets inclined 60° to the oncoming flow at high Reynolds numbers was examined in smooth flow conditions.

In Christiansen et al. (2017) the observed dynamic response was presented and the influence of the helical fillets on the mean aerodynamic loads as well as instantaneous loads in the drag crisis region was described and discussed. For the cable with helical fillets, large amplitude vibrations were shown to be dependent on the surface irregularities of the cable. Vibrations were only recorded for a cable rotation of $-90°$, and the focus is therefore kept on this axial rotation. Another important result to be referenced later in this paper was the appearance of single separation bubble instabilities in the form of jumps in between semi-stable boundary layer transition states and sudden bursts in between states. These instabilities were found in a lower Reynolds number region than where the large amplitude vibrations were recorded and could thus not explain the vibrations in this case. Also, the presence of the helical fillets were seen to displace the stagnation point towards the side of the cable with the helical fillet nearly aligned with the flow, in a periodic manner,

* Corresponding author.
  E-mail address: hch@sohansen.dk (H. Christiansen).
[1] Now at: Svend Ole Hansen Aps, Sankt Jørgens Allé 5C, 1615, Copenhagen V, Denmark.
[2] Now at: RWDI, 75 Albert Street, Suite 209, Ottawa, ON, K1P 5E7, Canada.

depending on the angular positions of the helical fillets.

As the title suggests, the objective of this paper is to study the fluctuating load and wake characteristics, to improve the understanding of the flow development around an inclined cable with helical fillets and the interplay between surface pressures, wake behaviour and cable velocity.

2. Experimental setup and measurements

For a description of the experimental wind tunnel test setup and measuring equipment reference is made to Christiansen et al. (2017) and Larose and D'Auteuil (2014). For the sake of readability of the following sections, the angular position of the helical fillets nearly normal to the flow are, however, shown in Fig. 1. The recording time is 90 s. The sampling frequency of the pressure transducers is 312.5 Hz and 2500 Hz for the Cobra Probe located in the wake of the cable model, downstream ring 3.

3. Results and discussion

3.1. Fluctuating load

3.1.1. Spectral distributions

The frequency content of the unsteady across-wind load coefficient, onwards referred to as the lift coefficient, will provide some insight into the loading mechanism on the cable. Power spectral densities (PSD) of the lift coefficient averaged over the four rings of pressure taps and the lift coefficient at each of the rings are presented in Fig. 2 for different Reynolds numbers. These are based on static tests to avoid motion effects on the forces. Considering first the four rings, the intensities of the lift force fluctuations vary between the rings as would be expected. The frequency distributions are broad-banded for all the Reynolds numbers shown in the figure, but in most cases with high spectral peaks at low frequencies.

For the Reynolds number of $1.27 \cdot 10^5$, parts of the lift coefficient time histories are shown in Fig. 3 for rings 1, 3 and 4, and in Fig. 4 for ring 2. The time histories show that the low frequency peaks generally were caused by separation bubble instabilities during the transition of the boundary layers from laminar to turbulent flow near the separation lines as described in Christiansen et al. (2017). Strictly, power spectral analyses are reserved for stationary signals only and not applicable for time series showing boundary layer instabilities. However, the high spectral low-frequencies serve as an indicator of this flow behaviour. No evidence of background noise was found in the measurements. For rings 3 and 4 where the largest low frequency forcing was found, the time series of the lift coefficient were not stationary and reveal that the instabilities were in the form of jumps in between semi-stable states due to the alternating formation and loss of a separation bubble (Fig. 3). On the other hand, the low frequency components for ring 2 were caused by bursts in the lift force (Fig. 4). Note that the helical fillets are located in the base and stagnation regions for ring 2 (Fig. 1), so the load characteristics are similar to those of a smooth cable. Surface pressure coefficient distributions for ring 2 at the three time instants a, b and c in Fig. 4, reveal that a separation bubble was established on the upper cable side, whereas a bubble seemed to alternately form and break down on the lower cable

side. The variation in magnitude of the suction on the upper cable side could indicate a variation in size of the separation bubble. Low frequencies could also be provoked by low frequency pulsation of the wind speed inside the test section which was observed for wind speeds below 14 m/s in outdoor gusty wind conditions.

As the Reynolds number was increased to $2.54 \cdot 10^5$ the low frequency components reduced with varying magnitude for the different rings (Fig. 2). At a Reynolds number of $3.73 \cdot 10^5$, low frequencies were pronounced for ring 1 and ring 2. Regarding the former, the taps located downstream of the helical fillet nearly normal to the flow were found to contain a high energy content of low frequencies through a study of the PSDs of the individual taps. The PSDs are not shown here, but reference is made to section 3.2 where a study of individual taps is made for ring 3. For ring 3, low frequencies of the surface pressure coefficients downstream the helical fillet nearly normal to the flow are shown to be dominant compared with the frequencies in the separation region on the smooth cable side where the helical fillet was near aligned with the flow. For ring 1, the helical fillet nearly normal to the flow is located 58° counterclockwise from tap 29 (see Fig. 1), thus significantly influencing the fluctuations of the lift, and makes the origin of the dominating low frequencies in Fig. 2. Regarding the low frequencies seen for ring 2 at Re $= 2.54 \cdot 10^5$ (Fig. 2) these are believed to be caused by the inherent varying size of the separation bubbles and varying angular position of the final separation point. At Re $= 3.73 \cdot 10^5$ the low frequencies could be caused by the same effects or they could be an indication of the disintegration of the separation bubbles, which for a smooth cable inclined to the flow has been suggested as fundamental for the initiation of large model vibrations by Jakobsen et al. (2012). However, it remains uncertain why these contributions would be so significant for ring 2 only. The difference could stem from surface irregularities or the angular position of the helical fillet. There was no clear peak at the cable natural frequency of 1.4 Hz (that established large amplitude vibrations in the dynamic tests) for any of the rings.

Besides the low frequency peaks there was also an indication of broad-banded higher frequency peaks in the PSD of the lift coefficient. These will be discussed further in the next section.

For the lift coefficient averaged over the four rings (Fig. 2 bottom) the large low-frequency components as seen for the individual rings at the low Reynolds number caused by bubble instabilities were retained. At the higher Reynolds numbers the low frequency peaks however cancelled out and the broad-banded high frequency peaks were prominent compared to the PSDs of the individual rings, suggesting a vortex shedding process. This will be studied further in the next section.

3.1.2. Vortex-shedding excitation

To capture the development of the vortex shedding process, contour plots were constructed from the PSDs at different Reynolds numbers and are shown in Fig. 5 for the averaged value over the four rings and in Fig. 6 for each of the four rings.

The vortex shedding process suggested is marked by the red dashed line in Fig. 5. It indicates periodically shed vortices with a shedding frequency linearly proportional to Reynolds number, corresponding to a Strouhal number of 0.19. The dimensionless Strouhal number is
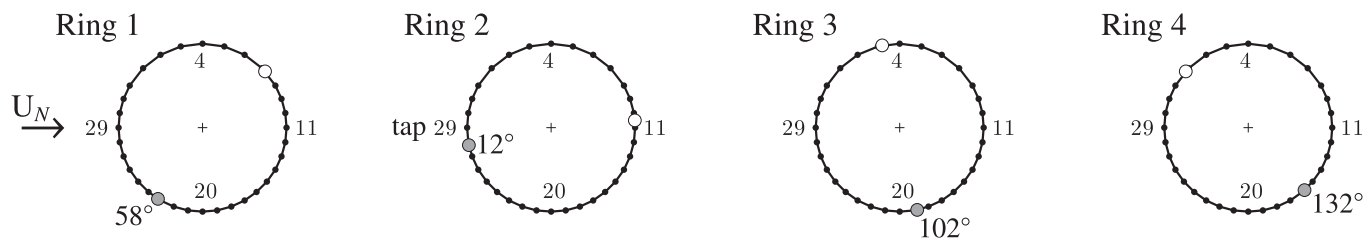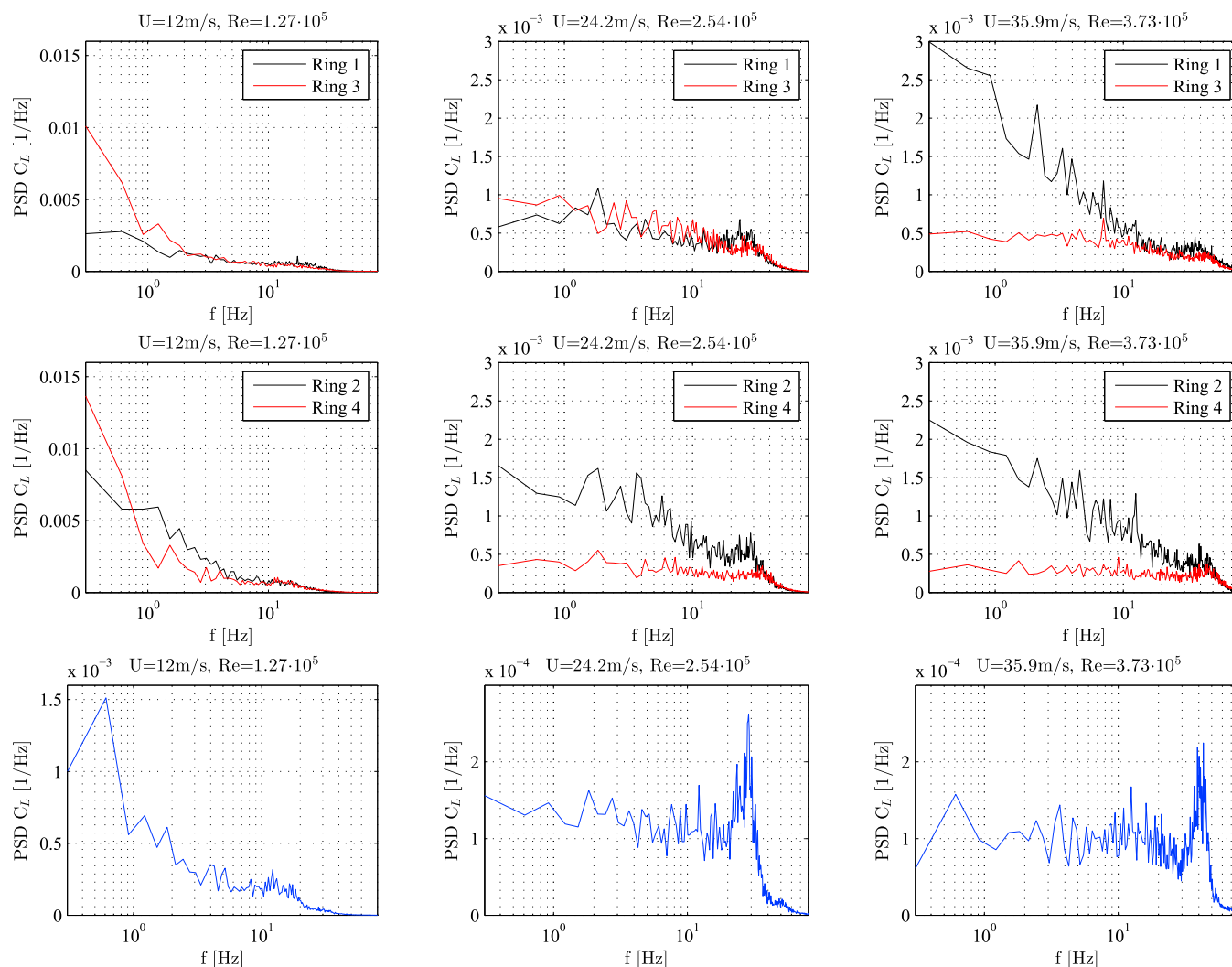

Fig. 1. Angular position of helical fillets nearly normal to the flow counterclockwise from tap 29 on the four rings of pressure taps at a cable rotation of $-90°$. ● fillet normal to the flow, ○ fillet aligned with the flow.

Fig. 2. Power spectral densities of lift coefficients for a cable rotation of $-90°$, top row: ring 1 and 3, middle row: ring 2 and 4, bottom row: averaged value over the four rings. Based on integration of surface pressure measurements of static tests. Mark the difference in the scale of the y-axis. (For interpretation of the references to colour in this figure legend, the reader is referred to the Web version of this article.)

determined as $St = f_v D / U = f_v D^2 / \nu Re$, where U is the oncoming free stream wind speed, f_v is the vortex shedding frequency and $\nu \approx 1.5 \cdot 10^{-5}$ m/s^2 is the kinematic viscosity of the air. Had the independence principle been applied i.e. using the component of wind normal to the cable axis, $U \sin\phi$, the Strouhal number would reach 0.22. Given the inherent three dimensionality of the flow on an inclined cable (see for example flow vizualisations by Andersen (2010)) the free stream flow speed U is used as a reference.

It is interesting to observe that vortex shedding in Fig. 5 persists throughout the entire Reynolds number range tested, even during flow transition, with a Strouhal frequency of 0.19. For a smooth cylinder in cross-flow, it has typically been reported that the classical von Kármán vortex shedding with St = 0.19 would disappear at the end of the subcritical regime. In the critical one-bubble regime a jump in the value of St to 0.32 would occur and in the supercritical two-bubble regime, vortices would initially be shed at a frequency nearly double the subcritical frequency corresponding to St = 0.46 and thereafter drop to a vortex shedding process with a Strouhal number between 0.20 and 0.30 (Zdravkovich (1997), Polhamus (1984)). For a cable normal to the flow with helical fillets, Kleissl and Georgakis (2012) identified a vortex shedding process with a Strouhal number of 0.20 which would cease to exist when the boundary layer underwent transition from laminar to turbulent flow. Fig. 5 therefore shows a different behaviour for a cable

inclined to the flow with helical fillets. However, vortex shedding at high Reynolds numbers has been reported in several other studies for a smooth cable. In the case presented in this paper the vortex shedding is better organised/correlated along the model span than the low-frequency part and is therefore a more visible part of the lift forcing averaged over the four rings. An analysis of the co-coherence of lift in section 3.1.3 illustrates this, as the positive values are the largest at the reduced frequency of about 0.2. The large amplitude cable vibrations, at 1.4 Hz, were recorded for Reynolds numbers larger than $3 \cdot 10^5$ where the energy is focused at the Strouhal frequency, as well as spread over a very broad-band of frequencies below the vortex shedding frequency.

The PSDs of the different rings, depicted in Fig. 6, reveal high energy levels in the low frequency range and a faint suggestion of a broad-banded vortex shedding process with Strouhal frequencies in the vicinity of the one recorded for the case of the averaged of the four rings. The frequencies at which the high frequency vortex shedding takes place are most clearly seen in Fig. 2 where a variation between the rings is found. This is in agreement with findings by Nebres and Batill (1993) who mapped a variation in the Strouhal number as a function of the angular position of a large scale circular perturbation fixed axially along the length of a nominally circular cylinder normal to flow. This trend was later confirmed by Ekmekci et al. (2012). The perturbation to cylinder diameter ratios tested by Nebres and Batill were between 0.5 and 10
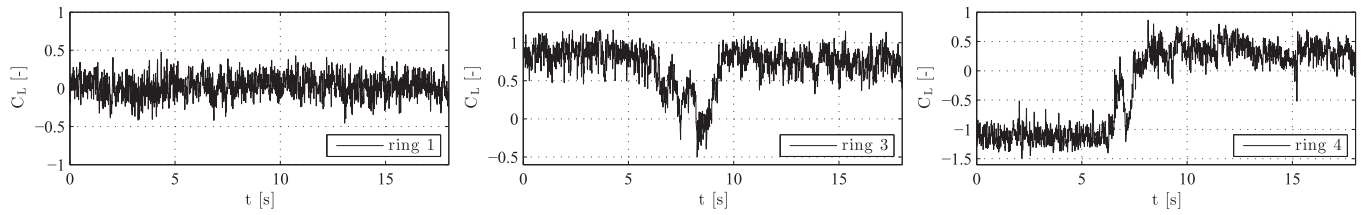
Fig. 3. Time series of lift coefficient C_L for ring 1, 3 and 4, displaying the unsteadiness in lift. Cable rotation of $-90°$, cable with helical fillets. Re = $1.27 \cdot 10^5$.
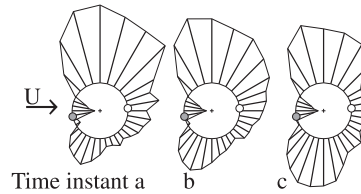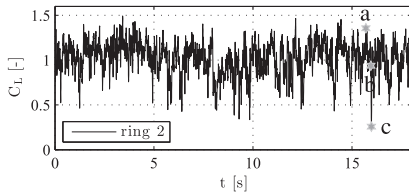

Fig. 4. Time series of lift coefficient C_L for ring 2, displaying the unsteadiness in lift, and pressure distributions at the marked time instants. ● fillet normal to the flow, ○ fillet aligned with the flow. Cable rotation of $-90°$, cable with helical fillets. Re = $1.27 \cdot 10^5$.
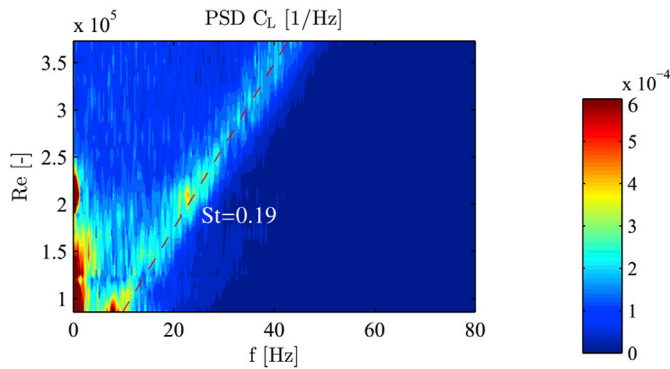

Fig. 5. Power spectral densities as a function of Reynolds number of the lift coefficients averaged over the four rings. Static case, cable with helical fillets, cable rotation $-90°$. (For interpretation of the references to colour in this figure legend, the reader is referred to the Web version of this article.)

times the value in the current experiments and the tests were at low Reynolds numbers of $1 \cdot 10^4$–$4 \cdot 10^4$, which showed a variation with Reynolds number. In the current test case a lower vortex shedding frequency was obtained for ring 1 compared with the other rings, corresponding to St = 0.16 (f = 35 Hz) at a wind speed of 36 m/s (Re = $3.73 \cdot 10^5$). For ring 2 the Strouhal number was approximately 0.18 (f = 40 Hz) and for ring 3 and 4 approximately 0.20 (f = 44 Hz). Comparing with the results of a cylinder diameter to wire ratio of 70 by Nebress and Batill (in the current tests 161.7 mm/2.4 mm = 67.5), the distribution of the Strouhal number as a function of the angular position of the perturbation do not coincide completely, with lower Strouhal number magnitudes for ring 1 and 2. The Reynolds numbers are however markedly different, and for the inclined cable with helical fillets the pressure tap rings are influenced by several stream lines. The vortex shedding frequency is related to the distance between the free shear layers before they roll up. The angular position of the helical fillets influence the local separation point and therefore the spacing between the free shear layers. The lower Strouhal number for ring 1 could thus be caused by an early separation directly at the helical fillet nearly normal to the flow at 58°, (Fig. 1), widening the wake. At rings 3 and 4 the helical fillets nearly normal to the flow were located further downstream at angular positions of 102 and 132°,
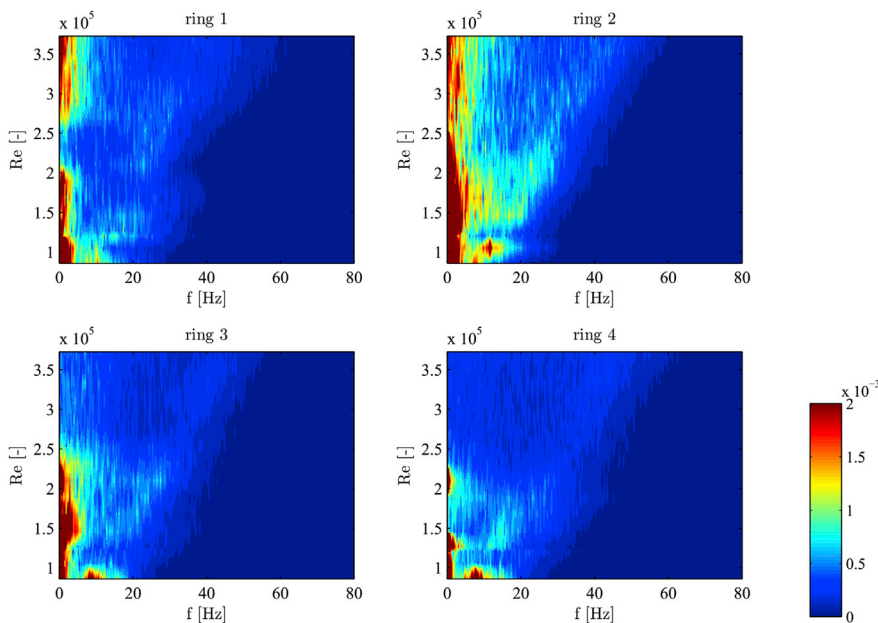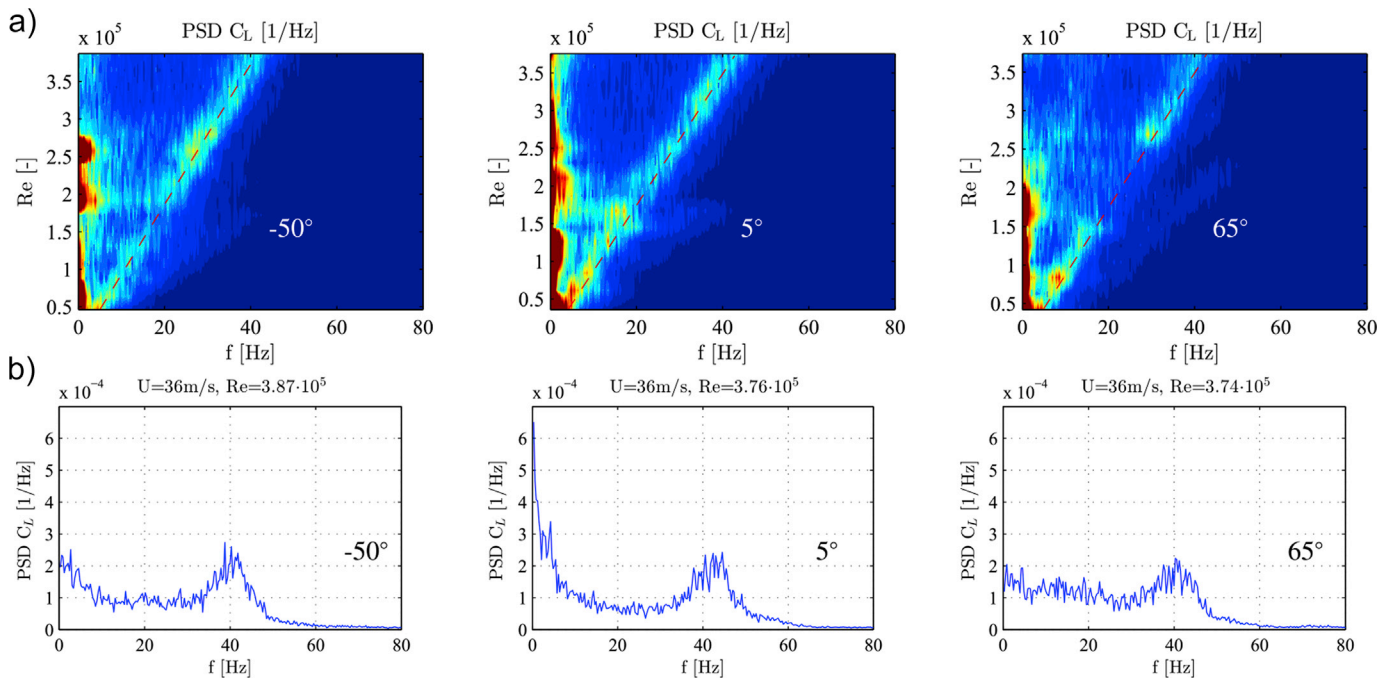

Fig. 6. Power spectral densities of the lift coefficients as a function of Reynolds number at the four rings. Static case, cable with helical fillets, cable rotation -90°, units: 1/Hz. (For interpretation of the references to colour in this figure legend, the reader is referred to the Web version of this article.)

Fig. 7. Power spectral densities as a function of Reynolds number of the lift coefficients averaged over the four rings for three cable rotations examined in dynamic cases for cable with helical fillets. (a) Contour plots. See Fig. 5 for colorbar. (b) PSD at a supercritical Reynolds number. (For interpretation of the references to colour in this figure legend, the reader is referred to the Web version of this article.)

indicating a narrowing of the wake and a higher vortex shedding frequency. (Surface pressure coefficient distributions for the four rings are shown in Christiansen et al. (2017) where approximate separation points can be seen). It is not clear why the Strouhal number at ring 2, with the helical fillets in the stagnation and base regions, is lower than rings 3 and 4. The separation points would be expected to lie in the same range, but the flow is highly three-dimensional.

In the high Reynolds number region above approximately $2.5 \cdot 10^5$ where the force coefficients are near constant, in the current tests, (see aerodynamic force coefficients in Christiansen et al. (2017) Fig. 6), most energy is located at frequencies below 10 Hz for ring 1 and 2, where the helical fillet nearly normal to flow is on the upwind side of the cable, and more broad-banded at ring 3 and 4 where the helical fillet nearly normal to flow is on the downwind side of the cable. Comparing with Fig. 5, it is interesting how the local frequency distributions with peaks of energy at lower frequencies cancel out to a large degree, leaving the vortex shedding process with $St = 0.19$ as the more prominent load at high Reynolds numbers. This indicates a span-wise variation of the lower frequencies

which is not coherent.

The frequency content of the fluctuating lift is shown for other cable rotations in Fig. 7. No static tests were made at these cable rotations, but given that no significant vibrations were observed they should provide a reasonable frame of reference for the comparisons. The high frequency vortex shedding was observed but in contrast to the cable rotation of -90° the magnitude of the Strouhal number varied for increasing Reynolds numbers. It must though be pointed out that an average over four discrete sections will not accurately represent the global forcing due to the inherent three-dimensionality of the flow of an inclined cable and due to changing angular positions of the helical fillets with axial rotations of the cable. It was also noticed that the lower frequencies were dominating throughout most of the Reynolds number range. This low-frequency contribution for the cable with a rotation of -90° was only present in the lower Reynolds numbers for the lift coefficient averaged over the four rings (Fig. 2) and not in the higher Reynolds numbers where the vibrations occurred. The low-frequency contributions could however also be caused by low amplitude oscillations.
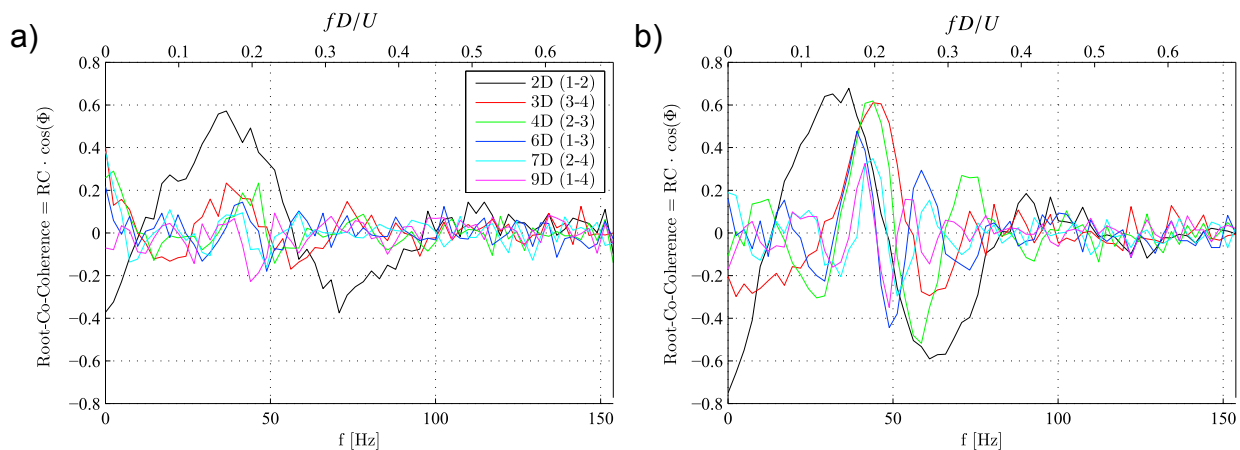
Fig. 8. Root-co-coherence of the drag (a) and lift coefficient (b) for $-90°$ cable rotation at Re $= 3.7 \cdot 10^5$, static case.
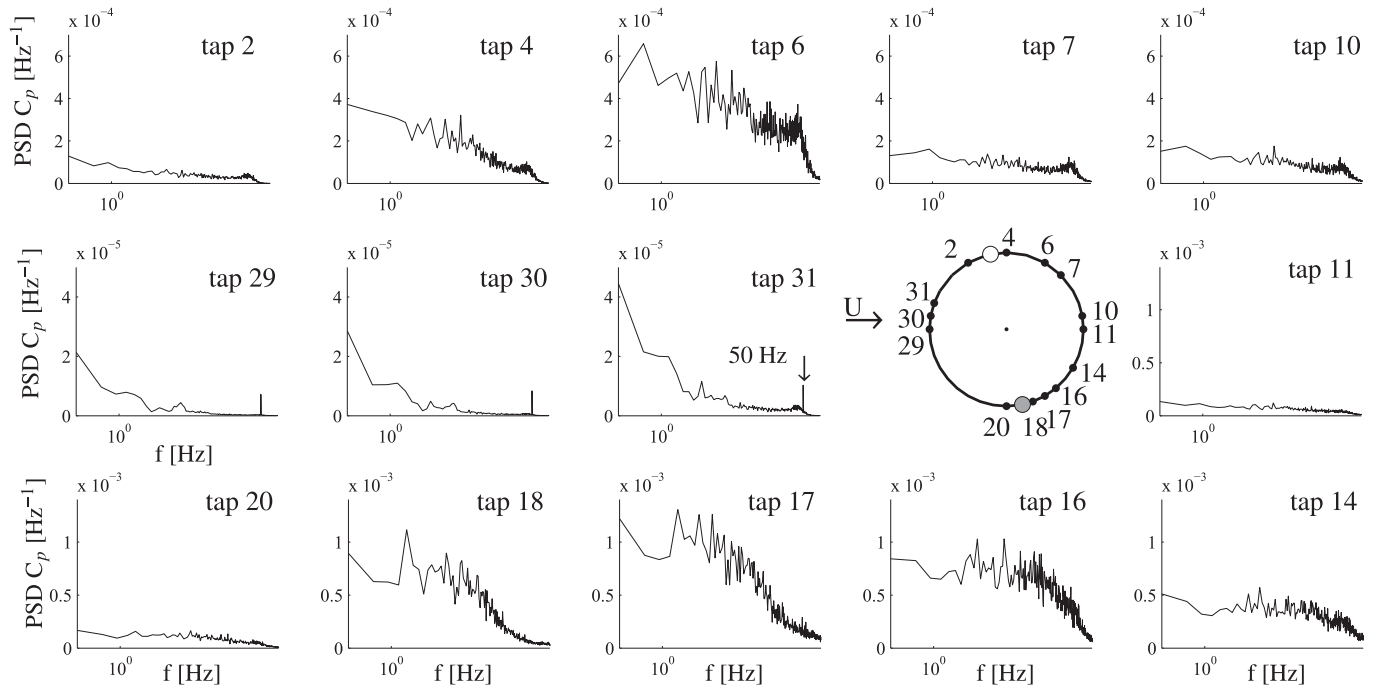
Fig. 9. Power spectral densities of the pressure coefficient at various pressure taps in ring 3 for a cable rotation of −90° at Re = 3.7·10⁵, static case. ●fillet normal to the flow, ○ fillet aligned with the flow. Mark the difference in the scale of the y-axis.

3.1.3. Coherence of the loading

The vortex shedding documented in Fig. 5 at a Strouhal number of 0.19 can be further examined in terms of the root-co-coherence function $RCC_C(f,s)$ of the lift force on the different rings (also called the normalized co-spectrum).

$$RCC_C(f,s) = \sqrt{Coh_C(f,s)}\cos \Phi(f,s) = \frac{|S_{CaCb}(f,s)|}{\sqrt{S_{Ca}(f)S_{Cb}(f)}}\cos \Phi(f,s) \qquad (1)$$

The root-coherence function $\sqrt{Coh_C(f,s)}$ is constituted by the PSDs of the lift coefficients $S_{Ca}(f)$ and $S_{Cb}(f)$ at the two locations a and b respectively, and the cross-spectral density $S_{CaCb}(f,s)$ where s signifies the distance between the two locations. The symbol Φ represents the phase angle. If the two signals are identical for a given frequency, RCC_C reaches the maximum value of one.

The root-co-coherence of the drag and lift coefficient for all combinations of rings are depicted in Fig. 8. For the lift coefficient, nearly all
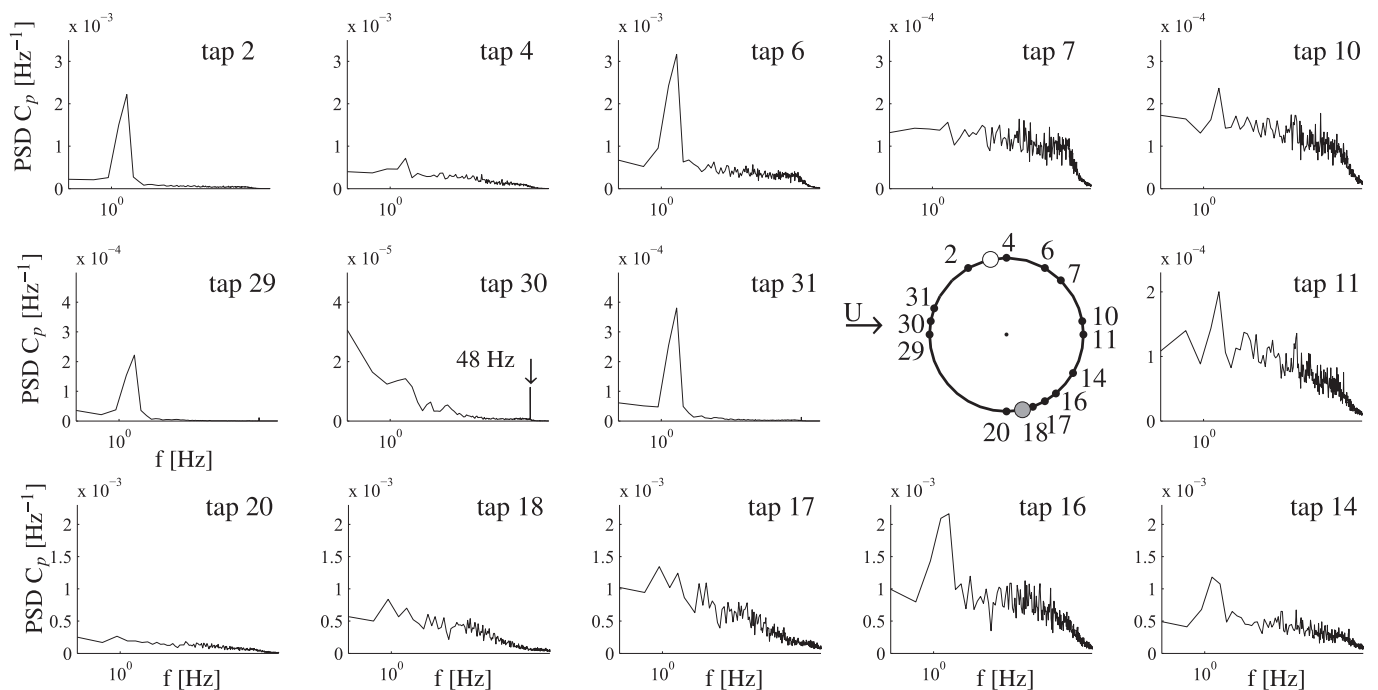
Fig. 10. Power spectral densities of the pressure coefficient at various pressure taps in ring 3 for a cable rotation of −90° at Re = 3.7·10⁵, dynamic case. ● fillet normal to the flow, ○ fillet aligned with the flow. Mark the difference in the scale of the y-axis.
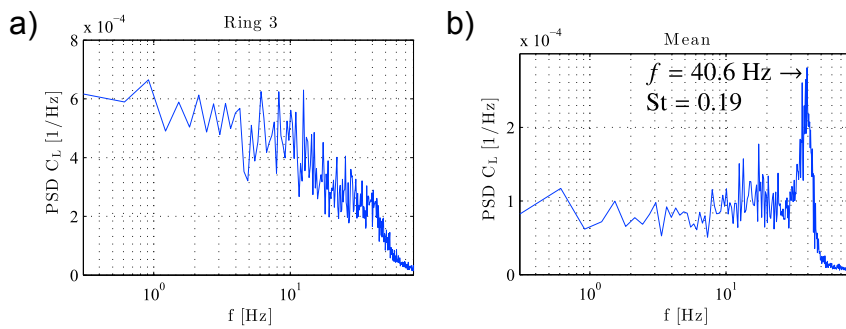
Fig. 11. Power spectrum densities of the lift coefficient in (a) ring 3 and (b) the average of all rings for a cable rotation of $-90°$ in dynamic case. $Re = 3.7 \cdot 10^5$.
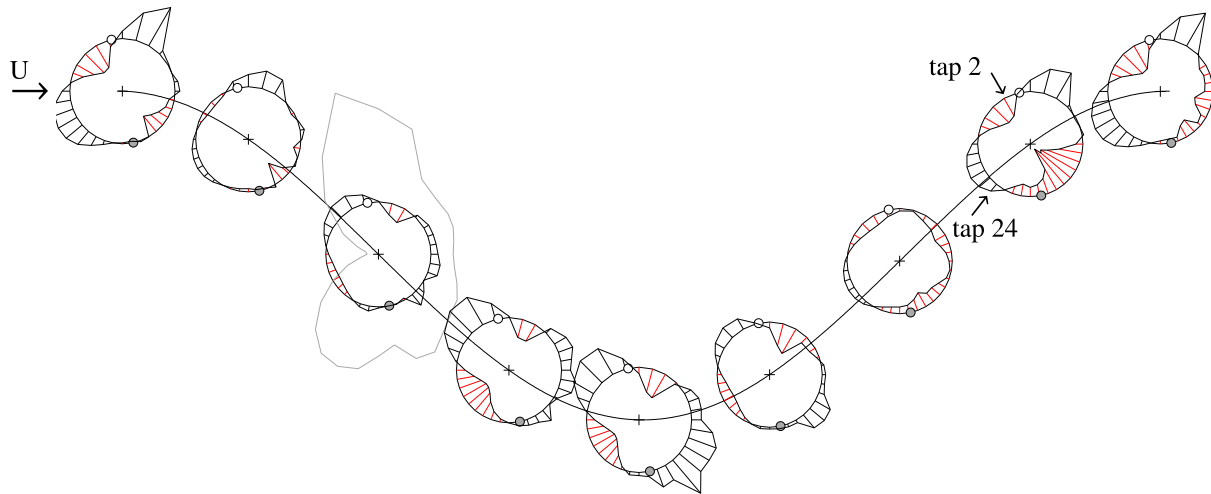

Fig. 12. Dynamic values between the instantaneous aerodynamic forcing averaged over the vibration cycles over a time interval of 40 s and the mean aerodynamic forcing. Gray silhouette shows the mean surface pressure coefficient distribution, with the cable radius corresponding to $C_p = 1$. Dynamic values scaled by a factor of 10. Cable rotation of $-90°$, ring 3, dynamic case, $Re = 3.7 \cdot 10^5$. ● fillet normal to the flow, ○ fillet aligned with the flow.
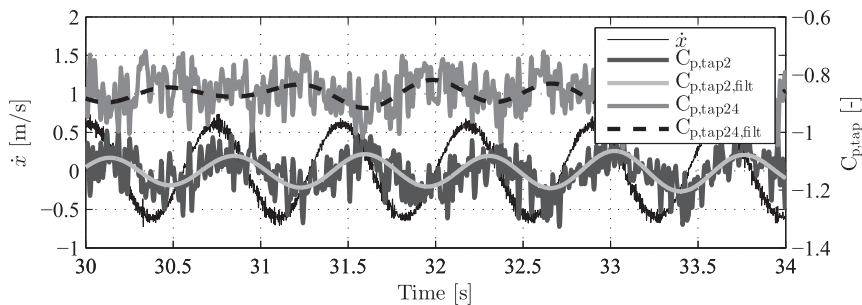

Fig. 13. Original and filtered time series of pressure coefficients in taps 2 and 24 and time series of cable velocity $\dot{x}$. Cable rotation of $-90°$, ring 3, dynamic case, $Re = 3.7 \cdot 10^5$. Suction is negative.

curves reach peak values around a Strouhal number of 0.19–0.20 where vortex shedding occurred, meaning that the loadings were well synchronized along the cable axis at this reduced frequency. Only the distance 2D was slightly displaced to lower Strouhal numbers. Also, as the distance between the rings increased, the band-width for significant root-co-coherence in the vicinity of $fD/U = 0.20$ became narrower and the root-co-coherence values smaller. The RCC_C for the drag coefficient reached a similar peak, although the values were smaller than 0.2 for all distances except the shortest distance of 2D. At various frequency ranges the RCC_C became negative for both lift and drag meaning that an increase in force for one of the rings was accompanied by a simultaneous decrease in force at the other ring. The loads were, in those frequency ranges, out of phase along the cable axis. Negative values have also been recorded on a smooth cable inclined 60° to the flow, Jakobsen et al. (2005), which stands in contrast to a smooth cable normal to the flow where the

coherence of forces is basically positive. For a cylinder in cross-flow, the mean flow component along the cylinder axis is absent and so is the source of a systematic propagation and delay of the flow structures along the cylinder span. The lift correlation, and thereby the underlying co-coherence, is thus positive and decreases with increase in the span-wise separation. Such a lift correlation on a smooth non-moving cylinder, and its dependency on the cylinder across-flow motion, has been studied by e.g. Wooton and Scruton (1970), as mediated in Dyrbye and Hansen (1999).

The curve representing the distance 2D between ring 1 and 2 separates itself from the rest of the curves. As pointed out in section 3.1.2, the frequencies of the broad-banded high frequency vortex shedding processes were lower for ring 1 and 2 than ring 3 and 4, resulting in lower Strouhal numbers as well. This difference was caused by the varying angular position of the helical fillet nearly normal to the flow and thus
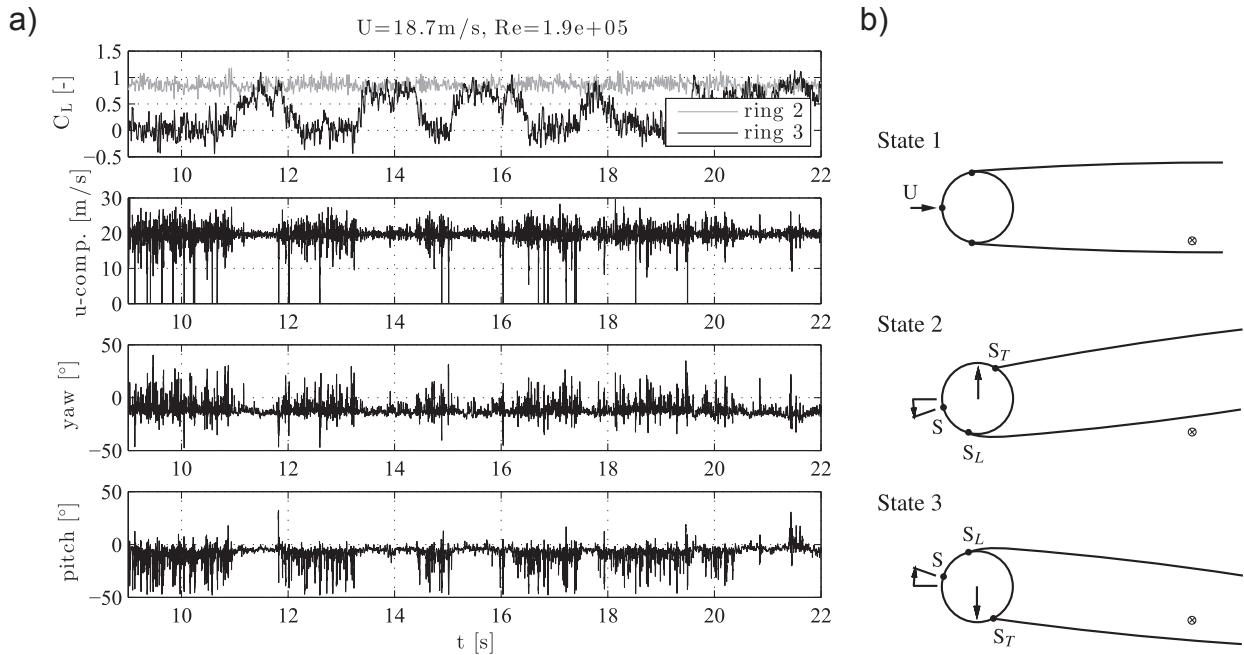
Fig. 14. (a) Cobra Probe measurements in the wake of the smooth cylinder. Yaw refers to flow variations in the wake in the horizontal plane and pitch is in the vertical plane. Static tests, axial rotation of $-93°$. (b) Sketch of states of the wake in the drag crisis region due to asymmetric pressure distributions. Cobra Probe marked by $\otimes$. S_L and S_T: laminar and turbulent separation points respectively. S: stagnation point.
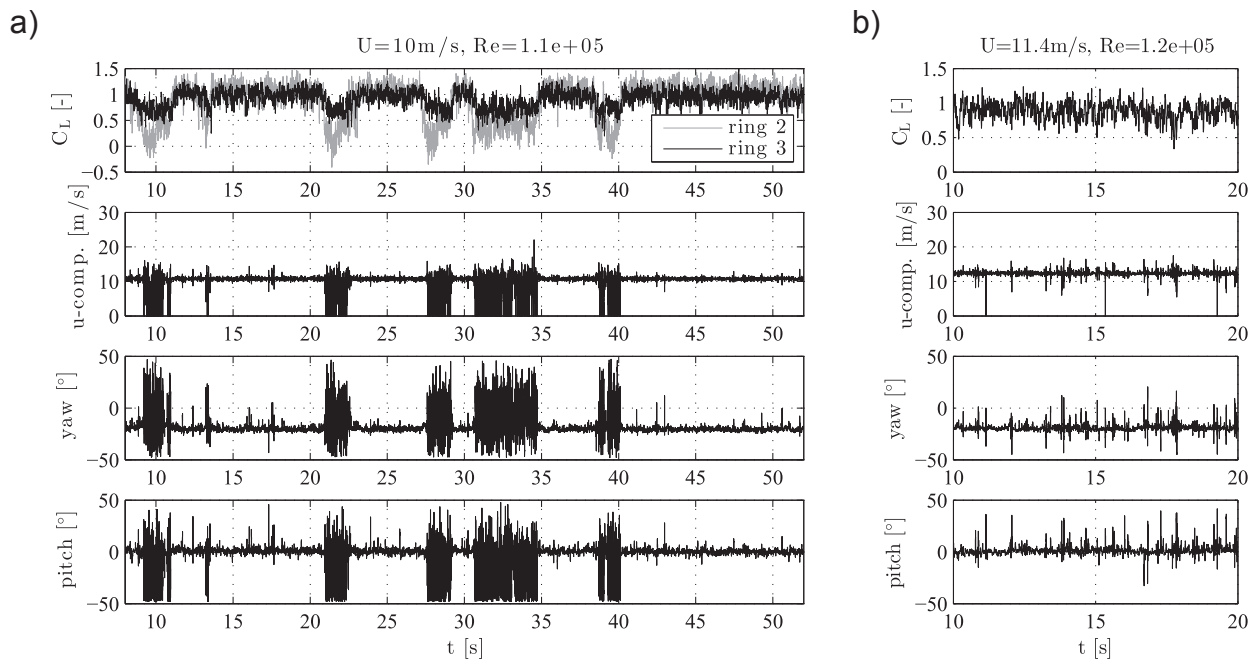
Fig. 15. Cobra Probe measurements in the wake of the cylinder with helical fillets. Static tests, axial rotation of $-90°$. (a) $\mathrm{Re} = 1.1 \cdot 10^5$, (b) $\mathrm{Re} = 1.2 \cdot 10^5$.

induced by the HDPE-tube geometry.

Model end effects could also have contaminated the flow at ring 1, but since the ring is located at a large distance of approximately 16D (2.5 m) along the length of the cable model from the wind tunnel ceiling this seems less likely. Nikitas et al. (2012) who worked with the same cable model in a previous test phase, concluded that end effects were not significant at the rings by comparing mean pressure profiles for two different end conditions. Studies by Matsumoto et al. (2001) also found the presence of high spectral low-frequency peaks near the upper end of a stationary cable model inclined 45° to the oncoming flow, which had

nearly vanished at a distance of 8D along the cable from the cable end at a free stream wind speed of 4 m/s i.e. $\mathrm{Re} = 1.3 \cdot 10^5$. This indicates that ring 1 is at a distance from the wind tunnel ceiling that should ensure uncontaminated data.

Another flow mechanism that can explain variation along the length of a cable, is the shedding of vortex cells in the along wind direction. The possible occurrence of this phenomenon will be discussed in section 3.3.1.

The lack of coherence at the cable natural frequency and the low magnitude of the PSD of the lift coefficients averaged over the four rings
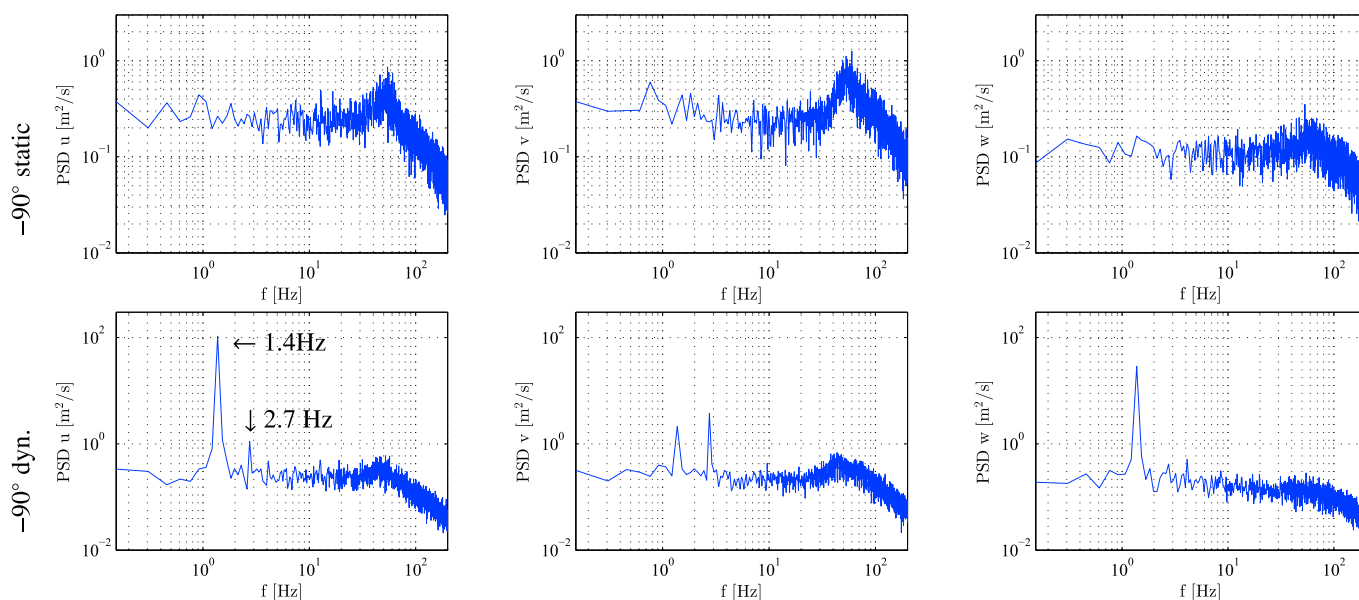
Fig. 16. Power spectral densities of Cobra Probe measurements in the wake for a cable rotation of −90° in both static and dynamic cases. Re = 3.7·10⁵.
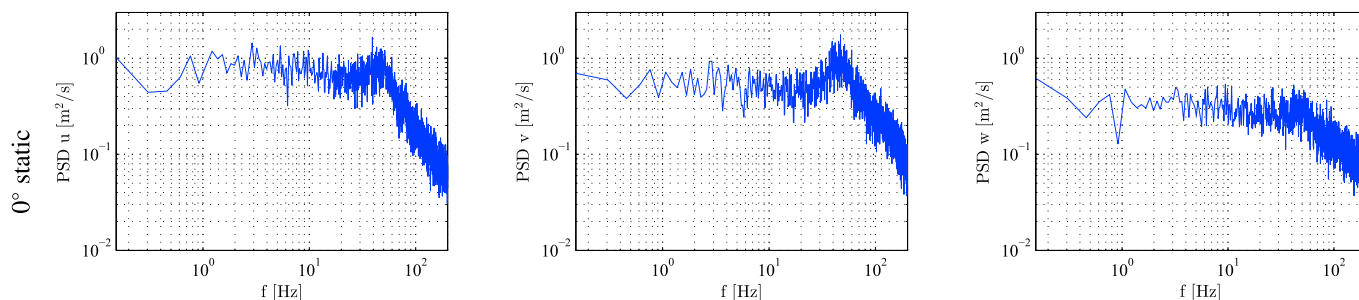

Fig. 17. Power spectral densities of Cobra Probe measurements in the wake for a cable rotation of 0° in static case. Re = 3.7·10⁵.

(Fig. 2) at this frequency for supercritical Re, could potentially suggest that the vibrations are not due to a pure resonant external aerodynamic forcing such as vortex shedding, but instead governed by a self-excited phenomenon.

3.2. Fluctuations of surface pressures

Zdravkovich (1997) argued that vortex shedding appears as periodic displacement of the stagnation point. Like vortex shedding, the velocity of the cable during motion is also expected to influence not only the stagnation point but most of the pressure distribution. To investigate this, the frequency content of the unsteady forces at different pressure taps is presented. Results for static and dynamic tests are shown for ring 3 in Figs. 9 and 10 respectively at the cable rotation of −90° for a Reynolds number of 3.7·10⁵ (the highest Reynolds number tested in the static case). The Reynolds number in the model tests is computed based on the oncoming free wind velocity, and the change induced by the cable velocity $\dot{x}$ in the dynamic tests is not considered. At the Reynolds number of 3.7·10⁵, for a mean wind speed of 35.9 m/s, the maximum cable velocity $\dot{x} = 0.7$ m/s. The relative wind speed varies between the free stream velocity U and $\sqrt{U + \dot{x}}$, resulting in a variation of less than 0.1%. The cable velocity would thus not introduce significant changes in the Reynolds number. It was shown by Christiansen et al. (2017) that the stagnation point of a cable with helical fillets is displaced towards the side of the cable with the helical fillet nearly aligned with the flow, so the results for taps 29, 30 and 31 are depicted (for a smooth cable the stagnation point would correspond to tap 29).

At the three taps in the stagnation region in the static test, a sharp peak is seen at 50 Hz with a sort of background broad-banded process (most clearly seen for tap 31) with frequencies resembling the vortex shedding process recorded for ring 3 in Fig. 2. The spectra are, however, dominated by high energy content in the low frequency region. The sharp 50 Hz peak was a product of the blade passing frequency, which is only visible in the stagnation region of the cable model since the boundary layer is not fully developed here. As the flow moves over the upper cylinder shoulder, where the helical fillet is near aligned with the flow, taps 2 and 4, the magnitude of the spectra increases. The broad-banded high frequency vortex shedding process remains. The largest energy contents on the smooth cable side are found at the final turbulent separation point, i.e. tap 6. Immediately behind this separation point the spectral magnitude has reduced, tap 7. On the side of the cylinder where the helical fillet is near normal to the flow, the highest spectral energies are located downstream of the helical fillet, taps 18, 17 and 16, and the high frequency vortex shedding process is barely visible. In the base region, the spectral magnitude has reduced again, tap 11. Similar spectra were retrieved for the other rings, although the distribution would vary with the angular positions of the helical fillet. At ring 2 for example, with the helical fillets in the stagnation and base regions (Fig. 1), the spectra on the two sides of the cable were similar in opposing pressure taps.

In the dynamic test notable spectral peaks are obtained at the natural frequency of the cable of 1.4 Hz for most taps, with the exception of taps located immediately downstream of a separation region, indicating an influence of the cable velocity on the pressures. In the stagnation region this distinct peak is seen for taps 29 and 31, whereas the PSD at tap 30 (mark the difference in the scale of the y-axis) is surprisingly like the
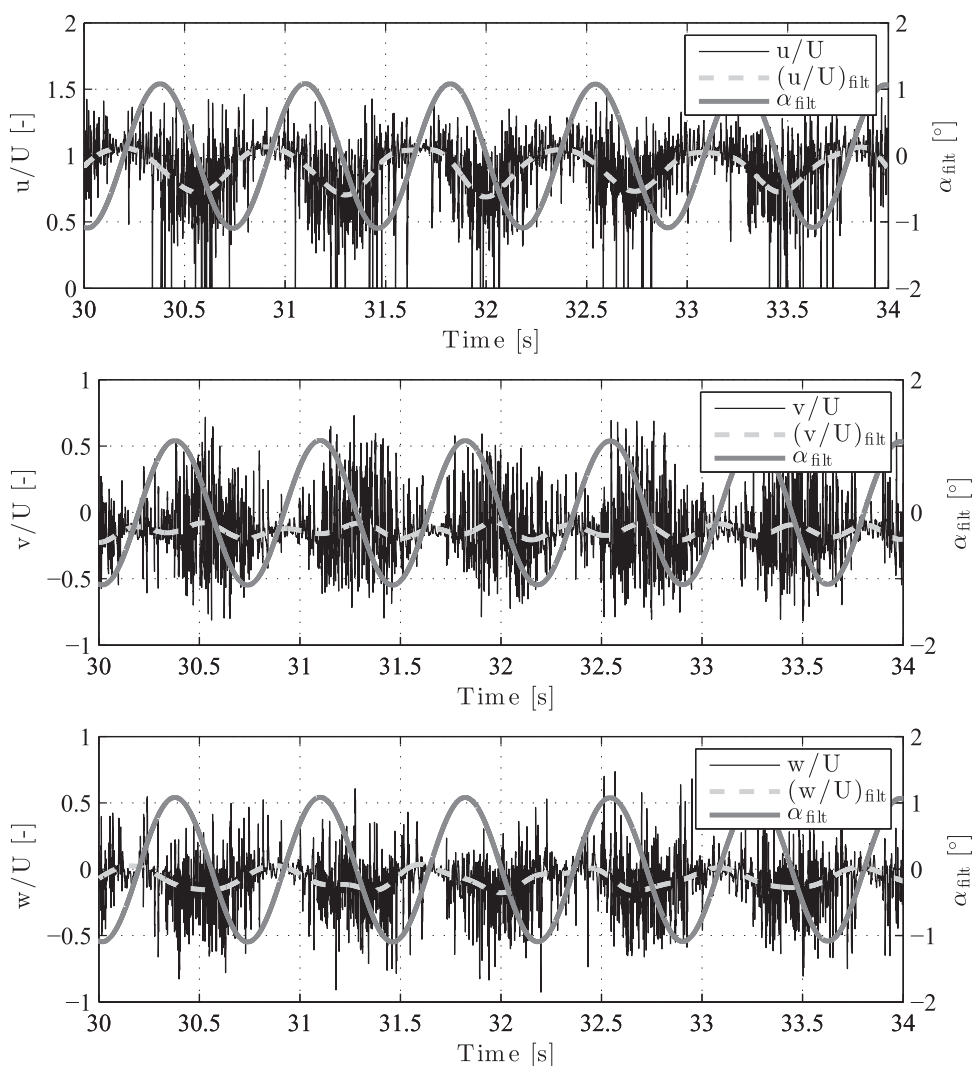
Fig. 18. Typical time histories of the ratio of the local velocities fluctuations to the free stream velocity and corresponding time histories of the effective wind angle-of-attack α. Cable rotation of $-90°$ in dynamic case at $Re = 3.7 \cdot 10^5$. Subscript 'filt' refers to band-pass filtered data.

static case although with an increase in energy at 1.4 Hz. The stagnation point is therefore expected to be in the vicinity of tap 30, but the mechanism is not easy to interpret. The blade passing frequency is here 48 Hz because of a slight decrease in wind speed (this also causes a reduction in Reynolds number which however is too small to be seen from the scientific notation). The blade passing frequency is clearly seen at tap 30, but it is also present at taps 29 and 31 although not as clearly visible because of the small magnitude compared with the spectral peak at 1.4 Hz. The high frequency vortex shedding process is still present but only to a minor degree. At ring 4, similar spectra were observed, whereas the peak at 1.4 Hz was more pronounced for rings 1 and 2. For ring 3, at taps 2, 4 and 6 on the smooth cable side where suction has developed, the pressure at the taps varies at the frequency of motion. The peak is reduced at tap 4 which was also the case at the other rings. This reduction could then be related to the line of laminar separation of the boundary layer. Immediately behind the line of turbulent separation on the smooth cable side, tap 7, the pressure is not significantly influenced by the motion of the cable but further downstream in the base region, tap 10, the motion becomes more apparent in the PSD. On the rough cable side immediately upwind and downwind of the helical fillet near normal to flow, tap 20 and 18 respectively, the PSDs display the appearance of high vorticity with no clear influence of the cable motion. Further downstream the cable motion becomes more pronounced, tap 16. Such high vorticity in the vicinity of this helical fillet was also recorded for the other rings; even ring 2 with the helical fillet in the base region.

For most taps, except immediately behind the separation point on the smooth cable side or behind a helical fillet near normal to flow, there is, in conclusion, a variation with the natural frequency of the cable of 1.4 Hz during motion. Considering the total lift coefficient of ring 3 and the lift coefficient averaged over the four rings there is, however, no distinct forcing at the natural frequency of the cable, Fig. 11. Since the variation of 1.4 Hz seen in the taps is a periodic motion of the pressure distribution around the cylinder circumference induced by the cable velocity during motion, the variation nearly cancels out when averaged over all taps. The variations between instantaneous surface pressure coefficient distributions over a vibration cycle and the time-averaged values were too small for a visual comparison of the two to be fruitful. The dynamic values are therefore shown in Fig. 12 displaying the periodic variation, scaled up ten times for visibility. The surface pressure coefficient distributions have been averaged over the vibration cycles over a time interval of 40 s. The periodic motion is most clearly seen on the smooth cable side, where a reduction in magnitude of the windward surface pressure coefficients was accompanied with an increase in magnitude of the leeward coefficients and vice-versa throughout the cycle.

Similar studies were carried out by Nikitas and Macdonald (2015) on a smooth cable inclined 60° to the flow in the critical Reynolds number region for $Re = 3.34 \cdot 10^5$, relating the change in surface pressure coefficient distribution to the cable velocity. The results stem from the same sectional cable model setup at NRC in a previous test phase in 2008. On

one side of the cylinder where a separation bubble had fully developed, the same behaviour as described above was observed resulting in a periodic motion of the surface pressure with the cable circumference. On the opposite side of the cylinder a separation bubble seemed to alternately form and break down leading to a strengthening and weakening of suction. Depending on the transition state in the boundary layer there thus seems to be different interactions between cable velocity and pressure distribution. Parallels can also be drawn to Zasso et al. (2005) where the pressure distribution from a nominally smooth circular cylinder normal to the flow was shown during lock-in of vortex shedding, clearly indicating a motion of the stagnation point. The cable model in the tests by Zasso et al. (2005) had a natural frequency of 3.25 Hz i.e. twice as large as in the present experiments and also reached higher amplitudes, reflecting the significant changes they saw in the pressure distribution.

It is noticed in Fig. 12 that as the cylinder velocity approaches zero, i.e. at max/min cable displacement, the dynamic pressure values are at their largest. The time series of the pressure coefficient for taps 2 and 24 are shown in Fig. 13 along with the cable velocity $\dot{x}$. The pressure coefficients in the two taps are in anti-phase in agreement with the results in Fig. 12. Keeping the focus on tap 2 the phase between C_p and the cable velocity is seen to be $80°$. For varying wind speeds the phase delay changed, but there seemed to be no clear correlation between the two. At the following three Reynolds numbers $3.91·10^5$, $3.92·10^5$ and $3.93·10^5$, where across-flow vibration amplitudes of around 0.47D were obtained (see Fig. 3 Christiansen et al. (2017)), the following phase lags were found: $80°$, $250°$ and $180°$ respectively, which show no clear pattern.

3.3. Wake characteristics

3.3.1. Wake characteristics during drag crisis

Schewe (1986) was the first to record the instantaneous jump in lift when a single separation bubble formed on either side of a nominally smooth circular cylinder normal to flow, when slowly increasing the Reynolds number. Oil flow photographs by Schewe (1986), on the walls of the wind tunnel test section between which the cylinder was mounted, also revealed a displacement of the wake field with the steady asymmetric surface pressures in the TrBL1 regime (i.e. the one-bubble regime using the nomenclature by Zdravkovich (1997)). Schewe described that the wake would displace towards the opposite direction than the stagnation point. Although not clearly written in the paper by Schewe, this should mean that the wake was oriented towards the same side as the lift i.e. the side where the single separation bubble would form, since the presence of a single separation bubble shifts the stagnation point towards the opposite cylinder shoulder (Kamiya et al. (1979)). In the following, this phenomenon is studied further as the wake flow structure at different boundary layer transition states is presented for the static cylinder based on the Cobra Probe measurements taken 2.5D downstream of the cable from the centre line at ring 3 and 5 mm inwards from the side of the cable with the helical fillet nearly normal to the flow.

The results for the smooth cable are presented in Fig. 14(a) for a more direct comparison with the results by Schewe and for the cable with helical fillets in Fig. 15. Only one static setup of the smooth cable model was tested which was for an axial rotation of $-93°$. In both figures, the instantaneous lift coefficient C_L at ring 3 is shown with the Cobra Probe measurements: the u-velocity component (along-wind direction), the yaw angle (the horizontal angle of the flow) and the pitch angle (the vertical angle of the flow). There is a clear correlation between the semi-stable states and the behaviour of the wake for both cables when experiencing state jumps. For the semi-stable states where $C_L \approx 1.0$, the u-component and the yaw and pitch angles measured in the wake are steady. The mean velocity of the u-component exceeds the mean free flow velocity U indicating that the probe is outside the wake. As an example $u/U = 19.6 \text{ m/s}/18.7 \text{ m/s} > 1.0$ for the smooth cable. The negative values of the yaw angles reflect the angle of rotation of the wake towards the positive lift direction, corresponding to state 2 in Fig. 14(b). The yaw angles were $-14°$ and $-20°$ for the smooth cable and the cable

with helical fillets respectively. The former is smaller than the latter due to a smaller magnitude of C_L.

For the semi-stable states where $C_L = 0$ for the smooth cable and $C_L = 0.65$ for the cable with helical fillets, the angle of the flow towards the Cobra Probe in yaw and pitch is larger/smaller than the measuring capacity of the probe of $\pm 45°$ providing results that are not reliable. The probe is expected to be in the wake in these semi-stable states. By observing other time series, this was found to be the case for all recorded lift coefficients up to 0.70, although dependent on the wind speed, which affects the width of the wake.

As for the steady asymmetric states reported in Schewe (1986), the wake for an inclined cable thus also displaces with the instantaneous jumps in boundary layer states. This can be divided into the three states shown in Fig. 14(b). The angular position of the stagnation point, and therefore the relative flow component, is thus the parameter controlling the direction of the wake. The separation points S_L and S_T represent the laminar and turbulent separation points respectively on a smooth circular cylinder, and are shown to highlight that the angular position of the separation points are not of prime importance in this matter. The principle of the direction of the wake field is therefore the same for a cable with helical fillets. As shown in Fig. 15(b) for Re $= 1.2·10^5$, the wake is even displaced for short increments of changes in the lift coefficient.

Another interesting observation is that the wake is at a vertical angle to the probe in the case of a smooth cable only. The pitch angle for the wake of the smooth cable is $-5°$ which tells us that the wake descends, i.e. it has a component of velocity in the direction of the cable axis. For the cable with helical fillets, the mean pitch was $0°$. A descending wake for the smooth cable corresponds well with the findings by Thomson and Morrison (1971) and Kleissl and Georgakis (2012) where vortex shedding cells were descending at an angle to the free stream flow. An inclined cylinder with a tapered free upstream end was studied by Thomson and Morrison (1971) who recorded the appearance of cellular vortex structures shed alternately from the cylinder shoulders after a short travel of the flow axially along the cable. A similar structure was presented by Kleissl and Georgakis (2012) from smoke vizualisations on a smooth cable inclined $45°$ to the flow. A channel of axial flow along the leeward side of the cable was captured, with discontinuous leakage into the wake forming some cellular flow structures. Smoke visualisations were also made by Kleissl and Georgakis on a cable with helical fillets, where the axial flow was nearly completely suppressed. Along-wind vortex cells were still created although not descending. More in-depth studies are however needed in order to confirm this theory as a $60°$ inclination angle also has been shown as a transition angle in between the appearance of cellular flow structures and unsteady vortex structures parallel to the cable axis by Polhamus (1984) for an ogive cylinder.

3.3.2. Spectral analysis

The Cobra Probe measurements taken 2.5D downstream of ring 3 provided time-dependent wind velocities in the three directions u (horizontally, along the oncoming wind direction), v (horizontally, transverse to the wind direction) and w (vertically). The frequency content of the u-, v- and w-velocity components may provide insight into the flow mechanisms and are therefore presented in Figs. 16 and 17 for cable rotations of $-90°$ (static and dynamics tests) and $0°$ (static test) respectively at Re $= 3.7·10^5$. As no significant vibrations were seen at a $0°$ cable rotation, only the static test is shown for this rotation. For the cable rotated $-90°$, a clear difference was observed regarding the development from the static to the dynamic test case. A broad-banded spectral peak can be observed at high frequencies for all three components of wind fluctuations in the static case. The broad-banded peak was at 50 Hz, which was slightly larger than the 44 Hz observed for ring 3 in Fig. 2, but corresponds to the blade passing frequency also seen for tap 29–31 in the stagnation region in Fig. 9. The broad-banded high frequency peak also appeared in the dynamic tests, but the spectral densities are dominated by a peak coinciding with the cable model natural frequency of 1.4 Hz
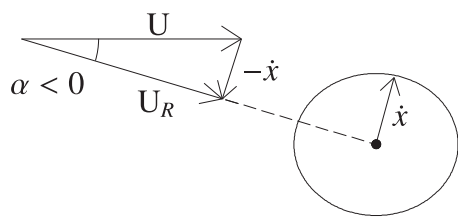
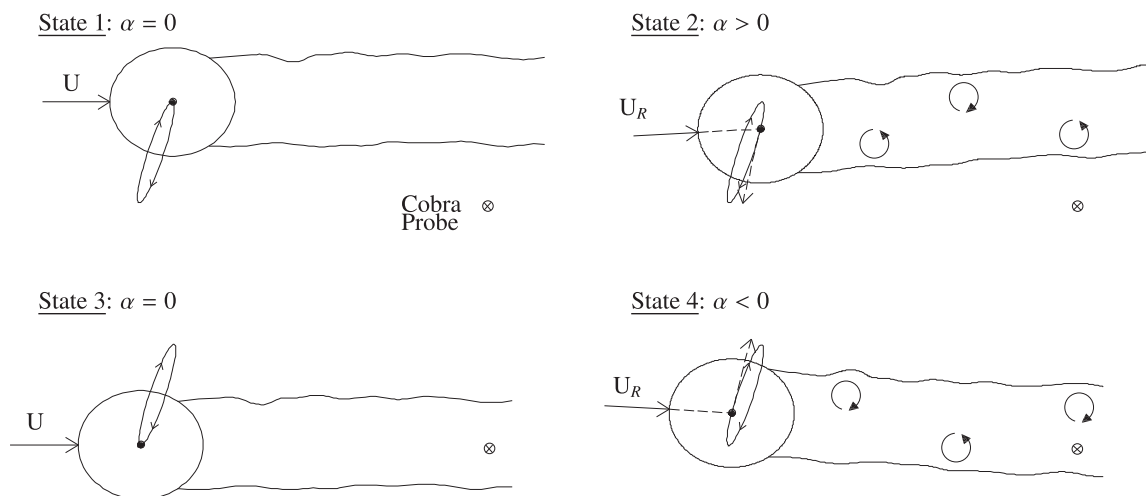**Fig. 19.** Velocities in a horizontal plane. $\dot{x}$ is the instantaneous direction of cable velocity.

and [1.05,1.8] Hz for the angle-of-attack data, using an 8th order Butterworth filter. The filtering process was performed by feeding the data first through a high-pass filter followed by a low-pass filter. To avoid phase distortion between the original and filtered signal, the data was processed both forwards and backwards. The analysis identified four different states of the wake field which are shown in Fig. 20. The motion trajectory of the cable model with an axial rotation of − 90°, was at an angle of 20° from the across-wind direction, explaining the motion trajectory in the figure. The motion was however not elliptical, but was drawn this way to clearly relate motion direction and effective angle-of-attack. The location of the probe in relation to the peak displacements of

Fig. 20. Wake fluctuations at different states in the translational orbit seen in a horizontal plane. Cobra Probe location marked as ⊗ .
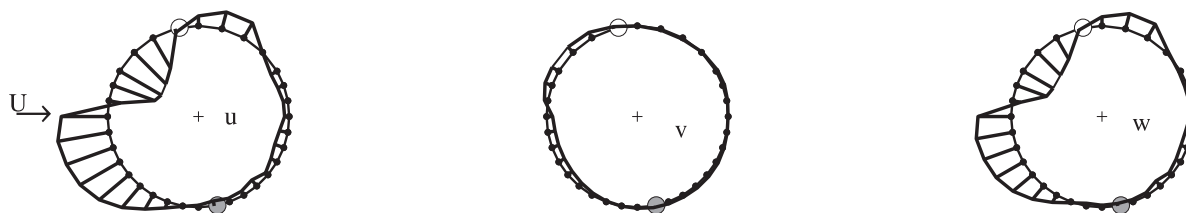

Fig. 21. Cross correlation between pressure coefficients at individual taps at ring 3, $C_{p,tap}$, and u-, v- and w-velocity components measured with the Cobra Probe in the wake. Cable rotation of − 90°, dynamic case. Cable radius equals a correlation of 0.5. fillet normal to the flow, ○ fillet aligned with the flow. Cobra Probe location: 2.5D downwind and 5 mm inwards from the side of the cable with the helical fillet nearly normal to the flow.

and a contribution from twice that frequency of 2.7 Hz for the $u-$ and $v-$ components. The spectral input at 1.4 Hz arose as the wake displaced periodically with the cable motion causing the Probe to be alternately enclosed in and free from the wake, which is shown in the following paragraph. The peak at 2.7 Hz is possibly caused by the shedding of vortices or the flapping of the separated shear layers alternating from each side of the cable in turns at a frequency of 1.4 Hz. Comparing the results at −90° cable rotation with results for a cable rotation of 0°, Fig. 17, the main difference was found in the higher spectral densities at low frequencies as was reported in section 3.1.2 for the PSD of the averaged lift coefficient over the four rings at rotations other than −90° (Fig. 7).

The time histories of the three velocity components measured with the Cobra Probe are presented in Fig. 18 relative to the free stream velocity U. The effective wind angle-of-attack α with respect to time is also shown with the sign convention as defined in Fig. 19. The time series have been "band-pass" filtered in the intervals [0.55,3.55] Hz for the Cobra Probe data, in order to include the frequencies of 1.4 and 2.7 Hz,

the cable model is shown as well in Fig. 20. Observing the u-component in Fig. 18, it is seen that as the effective angle-of-attack increased from approximately $-1°$ to $1°$, the cable was in the upper half of the translational orbit. Here, the velocity ratio $u/U > 1$ indicated that the Cobra Probe was free of the wake. As the effective angle-of-attack decreased and the cable was in the lower half of the translational orbit, the velocity ratio $u/U < 1$ indicated that the Cobra Probe was sheltered in the wake of the cable model. The wake therefore formed a roughly sinusoidal pattern downstream, with the different states shown in Fig. 20, which explains the spectral peak at 1.4 Hz seen in the PSDs in Fig. 16. As was the case for the measurements from the Cobra Probe in the static tests described in the previous section, the measuring capacity of the Probe was exceeded when the flow direction in yaw and pitch surpassed ±45°, which occurred when the Cobra Probe was enclosed in the wake. This caused the higher degree of fluctuation of the velocity components in those regions and it also seems to explain velocities of zero for the u-component.

3.3.3. Wake and surface pressure correlations

The correlation between the *u*-, *v*- and *w*-velocity components measured with the Cobra Probe and the surface pressures for the individual taps are depicted in Fig. 21 at high Reynolds number, $3.7 \cdot 10^5$. The correlation can be considered to be taken at the same time instant between the pressure taps and the Cobra Probe ports since the time for the flow to travel $2.5D$ to the Cobra Probe at 34 m/s is only 0.012 s. This minor time difference is not expected to cause significant changes in the correlation. The correlation was seen to have the same outline for the *u*- and *w*-components while the values for the *v*-component were of opposite sign and of smaller magnitude. This different behaviour of the *v*-component is in accordance with the results seen in Fig. 18.

The correlation plots demonstrate a clear relationship between the surface pressures and the velocity fluctuations in the wake. The correlations have the same outline as the dynamic phase averaged pressure coefficients shown in Fig. 12. As explained in section 3.2, the effective angle-of-attack varies with the cable velocity which causes the surface pressure distribution to more or less rotate relative to the cylinder circumference. The pressures in for example tap 2 and 24 (as shown in Fig. 13) will be 180° out of phase which will result in correlations of opposite signs to the wind velocities measured in the Cobra Probe. The largest correlations were found on the windward side of the cylinder and smaller correlations on the leeward side, indicating that the upstream pressure variations are most defining for the velocity fluctuations in the wake. It shall, however, be pointed out that the particular correlations shown are defined by the specific position of the Cobra Probe in the wake.

4. Concluding remarks

In static tests, the power spectral densities (PSD) of the lift coefficients at the individual rings were dominated by lower frequencies, which in the lower Reynolds number region were caused by separation bubble instabilities. There was also an indication of a broad-banded high frequency vortex shedding process, with local Strouhal numbers that were dependent on the angular position of the helical fillet nearly normal to the flow. When averaging the lift coefficients from the rings, the lower frequency peaks averaged out and left a vortex shedding process with a Strouhal number of 0.19 as the dominating load in the static case at high Reynolds numbers where large amplitude vibrations took place in the dynamic tests. It was interesting to observe that the vortex shedding process with St = 0.19 remained throughout the entire Reynolds number range tested and did not change in the critical Reynolds number region. Depending on the axial rotation of the cylinder, different results were however obtained. A low magnitude of the PSDs at the cable natural frequency and low coherence between the rings at this frequency suggested that the vibrations were not due to a pure external resonant aerodynamic forcing.

Fluctuations of the pressure coefficients at the pressure taps revealed high energy contents in the separation region on the smooth cable side and downwind of the fillet nearly normal to the flow on the rough cable side. In the dynamic tests, most taps had high frequency peaks at the natural frequency of the cable. An exception to this was the stagnation point with fluctuations resembling those of the static case and the taps in the vicinity of the helical fillet nearly normal to the flow and near the separation region on the smooth cable side. The peaks at the cable frequency revealed a periodic motion of the pressure distribution around the cylinder circumference, which did not seem to excite the cable.

A look into instantaneous wind velocity measurements $2.5D$ downstream of the cable in the wake in the static tests, revealed that the wake field changed direction with asymmetric surface pressure distributions and turned towards the same direction as the instantaneous lift force.

In the dynamic tests, a periodic displacement of the wake in phase with the motion of the cable model was also reported.

In light of the results presented in the these two companion papers, the authors remain puzzled about the excitation mechanism of the large amplitude vibrations recorded for the cable with helical fillets in the high Reynolds numbers. Using quasi-steady theory to explain the vibrations as galloping was not fruitful. Neither were the vibrations related to boundary layer instabilities in between the asymmetric and symmetric regimes. Although the analysis of the fluctuating loads in the rings of pressure taps in the static setup indicated otherwise, the vibrations at high Reynolds numbers were similar in character to high reduced velocity vortex shedding induced vibrations. For such vibrations, the low frequency excitations have been linked to the fluctuations of the axial flow and axial vortex cells that are amplified by the flapping shear layers due to vortex shedding. The experimental campaign repeated here did not provide full evidence that this was the case.

References

Andersen, T., 2010. Wind Load on Inclined Circular Cylinder in Drag Crisis. Faculty of Science and Technology, University of Stavanger. PhD Thesis UiS no. 118, Stavanger, Norway.

Christiansen, H., Jakobsen, J.B., Macdonald, J.H.G., Larose, G.L., Bosch, H., 2017. Aerodynamic stability of a dry inclined cable with helical fillets - Part I: stability and load characteristics. J. Wind Eng. Ind. Aerod. Submitted.

Dyrbye, C., Hansen, S.O., 1999. Wind Loads on Structures. Wiley.

Ekmekci, A., Aydin, T., Joshi, A., 2012. The control of flow past a circular cylinder via a single spanwise protrusion. In: International Conference on Flow-induced Vibrations, pp. 283–290 (Dublin, Ireland).

Flamand, O., 1995. Rain-wind induced vibration of cables. J. Wind Eng. Ind. Aerod. 57 (2–3), 353–362.

Jakobsen, J.B., Andersen, T.L., Macdonald, J.H.G., Nikitas, N., Larose, G.L., Savage, M.G., McAuliffe, B.R., 2012. Wind-induced response and excitation characteristics of an inclined cable model in the critical Reynolds number range. J. Wind Eng. Ind. Aerod. 110, 100–112.

Jakobsen, J.B., Andersen, T.L., Larose, 2005. Interpretation of wind forces monitored on an inclined stationary cylinder in critical Reynolds number range in relation to observed aeroelastic model response. In: 6th Int. Symposium on Cable Dynamics, pp. 287–294. Charleston, September.

Kamiya, N., Suzuki, S., Nishi, T., 1979. On the aerodynamic force acting on a circular cylinder in the critical range of the Reynolds number. In: AIAA 12th Fluid and Plasma Dynamics Conference, Williamsburg, Virginia, July 23–25.

Kleissl, K., Georgakis, C.T., 2012. Comparison of the aerodynamics of bridge cables with helical fillets and a pattern-indented surface. J. Wind Eng. Ind. Aerod. 166–176, 104–106.

Larose, G.L., D'Auteuil, A., 2014. Wind tunnel investigations on an inclined stay cable with a helical fillet. Report Number FHWA HRT-14-070. Federal Highway Administration, McLean, VA.

Matsumoto, M., Yagi, T., Shigemura, Y., Trushima, D., 2001. Vortex-induced cable vibration of cable stayed bridges at high reduced wind velocity. J. Wind Eng. Ind. Aerod. 89, 633–647.

Nebres, J., Batill, S., 1993. Flow about a circular cylinder with a single large-scale surface perturbation. Exp. Fluid 15 (6), 369–379.

Nikitas, N., Macdonald, J.H.G., Jakobsen, J.B., Andersen, T.L., 2012. Critical Reynolds number and galloping instabilities: experiments on circular cylinders. Exp. Fluid 52, 1295–1306.

Nikitas, N., Macdonald, J.H.G., 2015. Aerodynamic forcing characteristics of dry cable galloping at critical Reynolds numbers. Eur. J. Mech. B Fluid 49, 243–249.

Polhamus, E.C., 1984. A Review of Some Reynolds Number Effects Related to Bodies at High Angles of Attack. NASA contractor report 3809.

Schewe, G., 1986. Sensitivity of transition phenomena to small perturbations in flow around a circular cylinder. J. Fluid Mech. 172, 33–46.

Thomson, K.D., Morrison, D.F., 1971. The spacing, position and strength of vortices in the wake of slender cylindrical bodies at large incidence. J. Fluid Mech. 50, 751–783.

Wooton, L.R., Scruton, C., 1970. Aerodynamic stability, seminar on modern design of wind-sensitive structures. In: Construction Industry Research and Information Association. CIRIA, London, pp. 65–81.

Zasso, A., Manenti, A., Belloli, M., Giappino, S., Muggiasca, S., 2005. Energy input by the flow on a vibrating smooth circular cylinder in cross flow at Re=50000. In: 6th Int. Symposium on Cable Dynamics, pp. 299–306. Charleston, September.

Zdravkovich, M.M., 1997. Flow Around Circular Cylinders, vol. 1. Oxford University Press. Fundamentals.

Zuo, D., Jones, N.P., 2010. Interpretation of field observations of wind- and rain-wind-induced stay cable vibrations. J. Wind Eng. Ind. Aerod. 98, 73–87.